



Gas penetrating hollow fiber Bi with contractive bond enables industry-level CO₂ electroreduction

Aohui Chen^{a,b,c}, Xiao Dong^a, Jianing Mao^{b,d}, Wei Chen^{a,b,*}, Chang Zhu^{a,b}, Shoujie Li^a, Gangfeng Wu^{a,b}, Yiheng Wei^{a,b}, Xiaohu Liu^{a,b,c}, Guihua Li^{a,b}, Yanfang Song^{a,b}, Zheng Jiang^{a,d}, Wei Wei^{a,b,c,*}, Yuhan Sun^{a,b,c,*}

^a CAS Key Laboratory of Low-Carbon Conversion Science and Engineering, Shanghai Advanced Research Institute, Chinese Academy of Sciences, Shanghai 201210, PR China

^b University of the Chinese Academy of Sciences, Beijing 100049, PR China

^c School of Physical Science and Technology, ShanghaiTech University, Shanghai 201210, PR China

^d Shanghai Synchrotron Radiation Facility, Shanghai Advanced Research Institute, Chinese Academy of Sciences, Shanghai 201210, PR China

ARTICLE INFO

Keywords:

Bismuth hollow fiber
Gas penetrating electrode
Contractive bond
Conversion rate
Enhanced triphasic interface reactions

ABSTRACT

Electrochemical conversion of carbon dioxide (CO₂) to valuable fuels driven by renewable electricity exhibits significant potential for achieving carbon neutrality. Bismuth (Bi) possesses the reliable capability of electrocatalyzing CO₂ to formate, and high formate faradaic efficiencies have been realized over Bi-based catalysts, but industry-level large current densities with high conversion rates at mild conditions remain challenging yet. Herein we present a bismuth hollow fiber (Bi HF) as a gas penetration electrode (GPE) that efficiently reduces CO₂ with a formate faradaic efficiency of 93% and a current density of 1.13 A cm⁻² at -1.26 V (vs. RHE), corresponding to a CO₂ conversion rate of 37% under ambient temperature and pressure. Finite element analysis (FEA) and density functional theory (DFT) demonstrate that the synergetic combination of unlimited CO₂ feeding to triphasic interface reactions and selective reduction induced by contractive Bi-Bi bond is responsible for the superior activity of Bi HF.

1. Introduction

The electrocatalytic CO₂ reduction reaction (eCO₂RR) powered by renewable electricity is a promising technique for achieving carbon neutrality [1,2]. Tremendous efforts have been paid to reduce CO₂ into renewable fuels or value-added chemicals, for instance, C₁ products (CH₄, CO, CH₃OH, HCOOH) [3–6] and multicarbon products (C₂H₅OH, CH₃COOH, C₂H₄, C₂H₆, n-propanol) [7–10]. Even though C₂₊ products are more valuable, the high production cost resulting from their low selectivity and reaction kinetics, which could not satisfy the requirement of industrial scale implementation [11]. While recent technoeconomic evaluations show that the product of formic acid (or formate) or CO is feasible but more economical, they could be further upgraded chemically or electrochemically [12,13]. Formic acid is considered to be the most promising chemicals with the highest present value [14], as a hydrogen storage carrier applied to direct formic acid fuel cells [15–17].

Moreover, obvious virtues including easy availability, preservation, wide use as well as low toxicity of formic acid make it to be highly attractive [18–22].

In recent years, bismuth (Bi), as an earth-abundant low-price metal, has sparked great interest in eCO₂RR owing to excellent intrinsic capability of selective generation of formate/formic acid [23]. Designing and engineering Bi nanomaterials via active lattice plane exposures, defect decorations or surface structure modulations is considered an effective strategy to promote the eCO₂RR performance, and the faradaic efficiency (FE) of formate over prominent 2D Bi catalysts are generally exceeding 90% [24–26]. Moreover, Han et al. [27] and Yang et al. [28] reported that 2D Bi nanosheets showed ultra-high selectivity for formate formation (FE_{formate} = 100%). However, the current densities of producing formate over these Bi catalysts remain inferior due to limited mass transport from low CO₂ solubility and thick gaseous reactants diffusion boundary layer for planar electrode [29].

* Corresponding authors at: CAS Key Laboratory of Low-Carbon Conversion Science and Engineering, Shanghai Advanced Research Institute, Chinese Academy of Sciences, Shanghai 201210, PR China

E-mail addresses: chenhw@sari.ac.cn (W. Chen), weiwei@sari.ac.cn (W. Wei), sunyh@sari.ac.cn (Y. Sun).

<https://doi.org/10.1016/j.apcatb.2023.122768>

Received 7 November 2022; Received in revised form 29 March 2023; Accepted 12 April 2023

Available online 23 April 2023

0926-3373/© 2023 Elsevier B.V. All rights reserved.

One way for circumventing the above problems is using gas diffusion electrodes (GDEs) to enhance CO_2 accessibility to active sites [30–32]. Compared with conventional planar electrodes in H-type cell, the gaseous reactants are directly supplied to the catalyst layer in GDEs, where the gas diffusion path shortens dramatically, realizing sufficient gaseous feed in close proximity to the catalyst layer [33], thus the current densities of Bi-based catalysts using GDEs for eCO_2RR had been greatly improved [34–39] (Table S1). However, flooding exacerbates hydrogen evolution reaction (HER) with the losses of hydrophobicity and gas diffusion layers are highly prone to degradation due to carbonation for GDEs at high current densities [40], leading to the failure. Besides, the multiple components including active catalysts, binder and conductive additives in such GDEs were assembled to construct complicated structures by subtle procedures, decreasing the feasibilities of scale-up GDE applications. Different from GDEs, 3D hollow fiber of copper with distinct and compact hierarchical pore structures shows attracting advantages for efficient electroreduction of CO_2 by virtue of promoted mass transfer [41], the gas flow was all compelled to penetrate through the catalyst layer rather than the diffusion in GDEs. Thus, a steady high-concentration reactants at triphasic interfaces remains in such hollow-fiber configuration. Furthermore, this self-supporting electrode shows single active metallic component with well-integrated porous structures without any additives and binders, which can avoid from flooding and exhibits better structure stability. Recently, we achieved the efficient CO_2 reduction to CO at ampere-level current density ($>1 \text{ A cm}^{-2}$) by engineering the surface structure of silver hollow fiber [42]. However, to date for now, only copper-based hollow fiber electrodes were reported for formate product in eCO_2RR [43–46], and they deliver too limited current densities (less than 250 mA cm^{-2}) (Table S2) to satisfy industrial applications of formate production ($\geq 500 \text{ mA cm}^{-2}$). Hence, industry-level current densities and high CO_2 conversion rates to obtain formate from eCO_2RR at mild conditions remain a challenge yet.

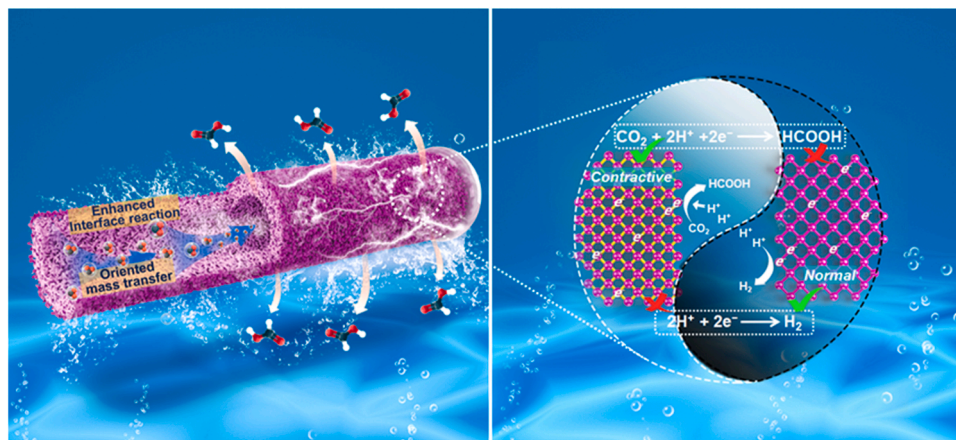
Herein, we present a Bi hollow-fiber gas penetration electrode (GPE) with micro/nanostructures, i.e., microporous integrated framework and nanosheet outer layer, both composed of only metallic Bi for efficient CO_2 electroreduction to formate. Over such Bi GPE, CO_2 molecules are forced to penetrate through highly porous walls of hollow fiber and continuously fed to active Bi nanosheets. Thus, both triphasic interface reactions and mass transfer kinetics are heightened (Scheme 1). Furthermore, the contractive Bi-Bi bond for Bi HF decrease the activation energy barrier of $^*\text{OCHO}$ key intermediate, facilitating CO_2 reduction kinetics while suppressing competitive HER (Scheme 1). As a result, a 93% FE and a 1.13 A cm^{-2} current density for formate in aqueous 2 M KHCO_3 at -1.26 V (vs. RHE) was achieved, corresponding to a CO_2 conversion rate of 37% at ambient temperature and pressure. This study means a large step forward in renewable CO_2 utilization.

2. Experimental

2.1. Preparation of Bi HF

The hollow-fiber $\text{Bi/Bi}_2\text{O}_3$ was fabricated by a combined phase-inversion/sintering process. Briefly, commercially available PEI (20 g) was added to NMP (70 g), followed by ultrasonic treatment for 1 h to obtain a homogeneous and transparent solution. Then Bi_2O_3 powder (110 g) was added into the above solution. As-obtained mixture was further treated by ball-milling (300 rpm) for 24 h to form a uniform slurry. After cool down to room temperature, the slurry was vacuumized (1 mbar) for 5 h to remove the bubbles and then obtain a casting liquid. Next, the casting liquid was extruded through the spinning machine and shaped in the tap water bath via the phase-inversion process. Directly after spinning the as-formed tubes were kept in a water bath for 24 h for completion of the solvent elimination, followed by drying and stretching for 48 h to obtain the green body. The whole fabrication of Bi HF involved only basic laboratory apparatuses under relatively mild conditions. The above fabrication process produced one batch of Bi_2O_3 green body with a total length of more than 150 m, demonstrating its high potential for scalable applications. The hollow-fiber green body was firstly cut into appropriate lengths and sintered in air flow (100 mL min^{-1}) at 550°C (heating rate: 1°C min^{-1}) for 6 h to remove PEI. After being naturally cooled to room temperature, the hollow-fiber Bi_2O_3 was partly reduced in hydrogen flow (100 mL min^{-1}) at 250°C (heating rate: 3°C min^{-1}) for 12 h with the dark outer surface, indicating the formation of metallic Bi. Subsequently, as-formed hollow-fiber $\text{Bi/Bi}_2\text{O}_3$ was further sintered in Ar flow (100 mL min^{-1}) at 720°C (heating rate: 1°C min^{-1}) for 6 h to obtain tough hollow-fiber framework with the completely fused metallic Bi and partly fused Bi_2O_3 . Then, the as-obtained hollow-fiber framework was calcined in air flow (100 mL min^{-1}) at 500°C (heating rate: 1°C min^{-1}) for 4 h to get pure Bi_2O_3 HF, and the inner and outer surfaces of hollow fiber showed a well-integrated substrate without spherical or granular particles and the Bi_2O_3 particles were sintered and fused to integral hollow-fiber base during the fabrication process. Finally, Bi_2O_3 HF was reduced in 0.1 M NaBH_4 solution (0.1 M NaOH) for 2 h to obtain $\text{Bi/Bi}_2\text{O}_3$ HF.

The $\text{Bi/Bi}_2\text{O}_3$ HF array comprising five $\text{Bi/Bi}_2\text{O}_3$ HF tubes. Each $\text{Bi/Bi}_2\text{O}_3$ HF tube, with an exposed length of 2.5 cm was stuck into a copper tube using conductive silver adhesive for electrical contact, while the end of the $\text{Bi/Bi}_2\text{O}_3$ HF tubes as well as the joint between the $\text{Bi/Bi}_2\text{O}_3$ HF and copper tube were sealed and covered with gas-tight and nonconductive epoxy. After drying at room temperature for 12 h, a working electrode was obtained with an exposed geometric area of 1.5 cm^2 ($S = \pi D_{\text{out}} L = 5 \times 3.14 \times 380 \times 10^{-4} \times 2.5 = 1.5 \text{ cm}^2$). Bi HF was synthesized from $\text{Bi/Bi}_2\text{O}_3$ HF by in situ electroreduction. Typically, the Bi HF GPE was subjected to reduction treatments on a Biologic VMP3



Scheme 1. Illustration of bismuth hollow fiber gas penetration electrode for boosting CO_2 electroreduction to formate.

potentiostat using a three-electrode system in a gas-tight two-compartment electrolysis cell with a Nafion 117 membrane as the separator, equipped with a KCl-saturated Ag/AgCl reference electrode and a platinum mesh (5 cm × 5 cm) counter electrode. The electrolyte solution was CO₂-saturated 0.5 M KHCO₃ and CO₂ specific flow rate remained 30 mL min⁻¹. Prior to the experiments, the electrolysis cell was vacuumized and then purged with CO₂ for 30 min. The Bi HF electrode was electrochemically reduction at a fixed potential of -0.3 V (vs. RHE) to obtain pure metallic Bi HF. The Bi HF electrode possessed the same exposed geometric area of 1.5 cm².

2.2. Synthesis of s-Bi HF

The synthetic procedure of s-Bi HF was that Bi/Bi₂O₃ HF was further reduced in 0.1 M NaBH₄ solution (0.1 M NaOH) to pure metallic Bi HF without electroreduction, the outer surface of s-Bi HF is smooth differing from that of Bi HF with abundant nanosheets.

2.3. Characterization

Scanning electron microscope (SEM) images were recorded on JSM-7800. X-ray diffraction (XRD) was recorded on a Bruker D8 Advance using Cu K α source ($\lambda = 1.54 \text{ \AA}$), which was examined before measurements to ensure the accuracy obeying the standard verification regulation using the silicon standard powder. In situ Raman measurements were carried out on a Raman spectrometer (i-Raman Pro BWS475-532 H, B&W Tek Corp.) using a 532 nm excitation laser with a laser power of 60 mW. Ex-situ Raman measurements of Bi/Bi₂O₃ HF and Bi HF were performed using the Micro-Raman Spectroscopy (Thermo Scientific DXR3xi) using a 532 nm excitation laser with a laser power of 5 mW. X-ray photoelectron spectroscopy (XPS) is performed using a Thermo Fisher ESCALAB 250XI, and prior to the XPS measurement of Bi HF the standard Ar⁺ etching pretreatment was conducted to remove as-formed oxide species due to the exposure in air. Curve fitting is performed using the Thermo Advantage software. The spherical aberration-corrected high-resolution high-angle annular dark-field STEM (HAADF-STEM) images were acquired by using a cold FEG JEOL Grand-ARM 300 F (JEOL, Tokyo, Japan) operated at 300 kV. Nuclear Magnetic Resonance (NMR) spectra were recorded by Bruker Advance III HD500. The XAFS measurements at Bi L₃-edge in the transmission mode were performed at BL14W1 station in Shanghai Synchrotron Radiation Facility (SSRF). For N₂ adsorption, the standard degassing station of the Mack instrument was used, and the samples were pretreated under the condition of vacuum 300 °C for 7 h, and then the samples were tested for nitrogen adsorption and desorption under the condition of 77 K liquid nitrogen using a Quantachrome Autosorb IQ3 automatic specific surface area analyzer. Gas permeation tests were performed with a custom gas permeability test system that could record the permeability of N₂ through the hollow fiber under different transmembrane pressure drops (see Supporting Information for more details). The inductively coupled plasma optical emission spectrometry (ICP-OES) tests were performed on a Thermo Fisher iCAP PRO with a 0.02 ppm detection limit for Bi³⁺ using RF Power under 1150 W, a plasma flow of 0.5 L min⁻¹, an auxiliary flow of 0.5 L min⁻¹, a nebulizer flow of 12.5 L min⁻¹, and a sample uptake delay of 30 s

2.4. Electrocatalytic reduction of CO₂

The potentiostatic electroreductions of CO₂ over all electrodes were performed at ambient temperature and pressure on the Biologic VMP3 potentiostat using the gas-tight electrolysis cell, which comprised two symmetrical compartments made of quartz glass with an inner height of 5.0 cm, an inner length of 5.0 cm and an inner width of 1.5 cm. The cathodic and anodic compartments were separated by a Nafion 117 membrane, and the electrolysis cell was equipped with a KCl-saturated Ag/AgCl reference electrode in the cathodic compartment and a

platinum mesh counter electrode in the anodic compartment. CO₂-saturated KHCO₃ aqueous solutions with different concentrations were used as the electrolyte solutions, which were cycled and refreshed in both the cathodic and anodic compartments at a flow rate of 30 mL min⁻¹ by using two identical peristaltic pumps (Jihpump BT-50EA 153YX). Under the similar electrolysis conditions, CO₂ flow rate of lower than 5 mL min⁻¹ resulted in very low formate faradaic efficiency and CO₂ conversion rates. While both the formate faradaic efficiency and CO₂ conversion rate increased rapidly when CO₂ flow rate was larger than 5 mL min⁻¹, and up to 30 mL min⁻¹. Further increasing the CO₂ flow rate to more than 30 mL min⁻¹ led to the slow increase of formate faradaic efficiency and the rapid decrease of CO₂ conversion rate. In order to obtain both appropriate formate faradaic efficiency and CO₂ conversion rate, the CO₂ flow rate was fixed at 30 mL min⁻¹ during CO₂ electroreduction unless otherwise stated. In the situations with very large currents (>400 mA), the Biologic VMP3 potentiostat was connected to a VMP3 booster chassis with an option of 10 A current.

2.5. Product quantifications and calculations

The details for Product quantifications and calculations are provided in the [supporting information](#).

3. Results and discussion

Bismuth oxide Hollow fiber (Bi₂O₃ HF) was prepared by phase inversion and calcinating processes at first from commercially available Bi₂O₃ powder, then followed by a wetting chemical reduction to bismuth/bismuth oxide hollow fiber (Bi/Bi₂O₃ HF) and subsequent in situ electrochemical reduction to completely pure-metal-phase bismuth hollow fiber (Bi HF) (Fig. 1a). Typical scanning electron microscopy (SEM) images showed that Bi₂O₃ HF possessed characteristic finger-like void structures from the cross-section view in the inner region (Fig. 1b), and molten Bi₂O₃ particles rather than dispersive globular ones in raw Bi₂O₃ powder (Fig. S1) consisted of a well-integrated outer surface of Bi₂O₃ HF (Fig. S2a), implying tough self-supported framework porous structures formed through the calcination during the fabrication of Bi₂O₃ HF. After the chemical reduction, the surface of Bi/Bi₂O₃ HF showed no distinct changes (Fig. 1c) compared with that of Bi₂O₃ HF (Fig. S2), while characteristic peaks of metallic Bi appeared in Bi/Bi₂O₃ HF besides Bi₂O₃ peaks from X-ray diffraction (XRD) patterns (Fig. 1e), indicating that Bi₂O₃ was partly reduced to Bi. Due to the presence of some metallic Bi, Bi/Bi₂O₃ HF was able to be further subjected to in situ electroreduction in 0.5 M KHCO₃ monitored by operando Raman spectra (Figs. 1d and S3). The intensities of Raman bands at 125, 345 and 495 cm⁻¹ corresponding to the A₁(1)+B₁(1), A₁(2) and A₁(3) modes of β -Bi₂O₃ [47,48], respectively, gradually decreased and finally vanished, indicating the transition of rest Bi₂O₃→Bi and the complete formation of Bi HF. While the Raman bands around 71 and 95 cm⁻¹ corresponding to the E_g and A_{1g} modes of metallic Bi were overlapped with these Bi₂O₃ peaks at the region from 70 to 180 cm⁻¹, which remained constant during the whole in situ electroreduction. Compared to the corresponding ex situ Raman peaks (Fig. S4), the broadened and blueshifted Raman peaks of Bi/Bi₂O₃ HF from 70 to 180 cm⁻¹ comprising the overlapped bands of metallic Bi and Bi₂O₃ was attributed to the effect of solvent water (Figs. S5 and S6). The broadening Raman bands modulated by water in the last three spectra in Fig. 1d remained almost coincident and were all assigned to the only metallic Bi component (Fig. S5a), implying the complete formation of Bi HF. XRD (Fig. 1e) and X-ray photoelectron spectroscopy (XPS) (Fig. S7) results verified that the bulk and surface compositions of Bi HF were identical with metallic bismuth. Interestingly, the smooth surface morphology of Bi/Bi₂O₃ HF (Fig. 1c) changed greatly to abundant vertically aligned nanosheets covered at the outer surface of Bi HF (Fig. 1f and Fig. S8). Moreover, a representative spherical aberration-corrected high-resolution high-angle annular dark-field scanning transmission electron

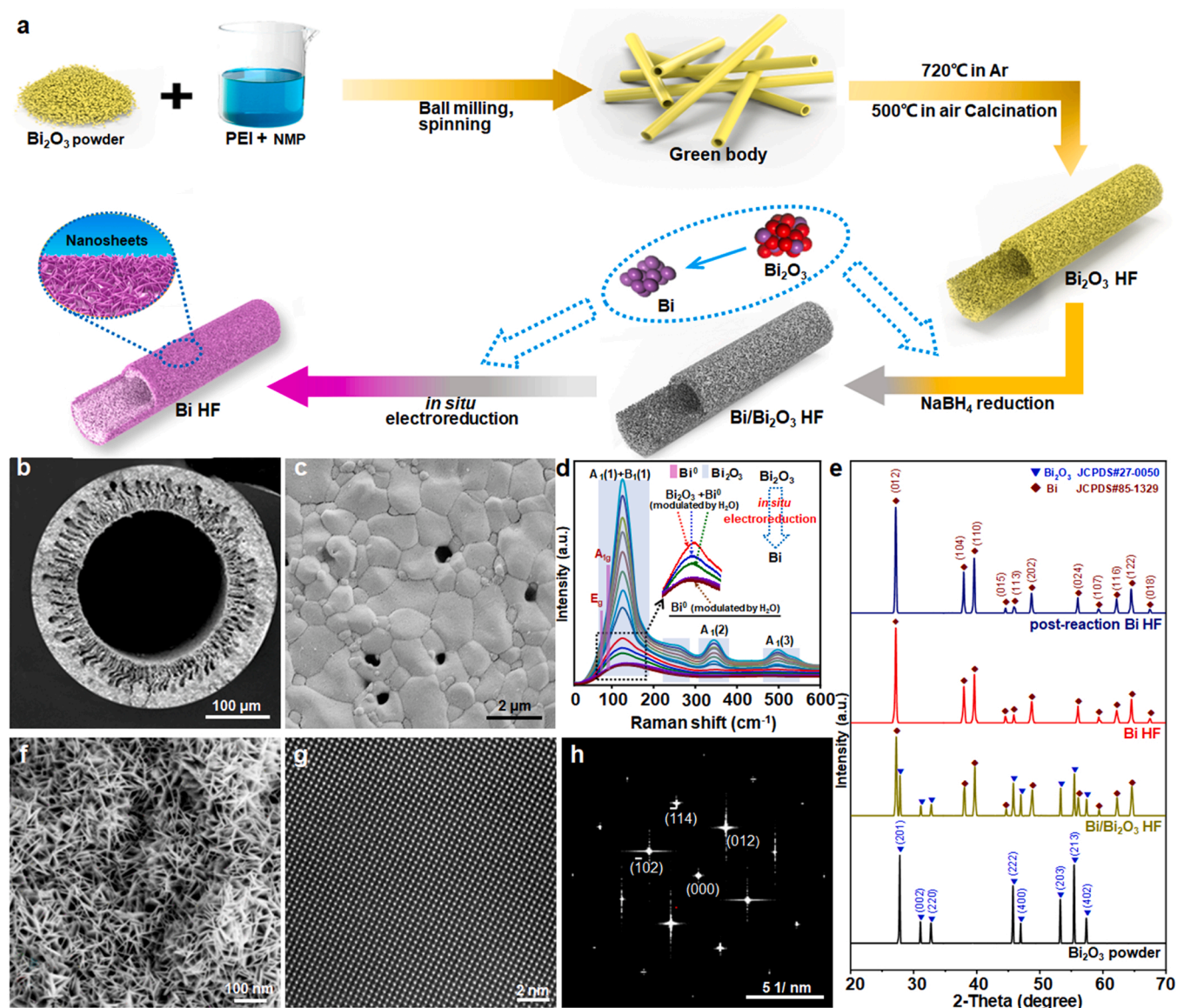


Fig. 1. Preparation and compositional characterization. (a) Schematic illustration of the preparation of Bi HF. SEM images of (b) Bi_2O_3 HF cross-section, (c) $\text{Bi}/\text{Bi}_2\text{O}_3$ HF outer surface, and (f) Bi HF outer surface. (d) Operando Raman spectra showing the composition change in situ electroreduction process of $\text{Bi}/\text{Bi}_2\text{O}_3$ HF to Bi HF with only metallic Bi reserved. (e) XRD patterns of all samples. (g) HAADF-STEM image and (h) FFT pattern of Bi HF.

microscopy (HAADF-STEM) image of Bi HF (Fig. 1g) showed the well-organized honeycomb lattice, confirming the relatively high crystalline quality for Bi HF, and the selected-area fast Fourier transform (FFT) patterns (Fig. 1h) matched well with the electron diffraction patterns of typical hexagonal system, displaying a set of diffraction spots with the $[2\bar{2}1]$ zone axis, which indicates the formation of single-crystalline Bi. These results evidenced that the basal plane of Bi HF was terminated with the (012) facet as expected, in consistent with XRD (Fig. 1e).

For comparison, metallic Bi hollow fiber with smooth surface (denoted as s-Bi HF) was obtained by only the wetting chemical reduction from Bi_2O_3 HF and $\text{Bi}/\text{Bi}_2\text{O}_3$ HF without the electrochemical reduction treatment (Fig. S9). The surface of s-Bi HF was similar to that of Bi_2O_3 HF and quite smooth, which was completely different from that of Bi HF (Fig. S10). Although the surface morphologies of Bi HF and s-Bi HF were completely different, their whole pore structures including average pore size and porosity obtained from gas permeability measurements were comparable (Table S3). In addition, N_2 adsorption and desorption results also showed the similar pore structures of the powders

derived from grinding Bi HF and s-Bi HF, respectively (Fig. S11). Moreover, XRD pattern (Fig. 2a) of both Bi HF and s-Bi HF showed obvious characteristic peaks at 27.2° , 37.9° and 39.6° , corresponding to the (012), (104) and (110) facets of pure metallic Bi, respectively. Interestingly, the peak for Bi HF appeared distinctly shift to high degree in comparison to those of s-Bi HF and ref. Bi (Fig. 2a), which indicates the compression of the unit cell [49]. Note that the (012), (104) and (110) peaks of s-Bi HF and Bi HF were broader than those of ref. Bi with an average size of $10\ \mu\text{m}$ (Fig. 2a), which was derived from the broadening diffraction peak effect induced by the nanosheet-covered surface of Bi HF and the smaller crystal surface/framework of s-Bi HF [50,51]. Furthermore, Bi $L_{3\text{-edge}}$ X-ray absorption fine structure (XAFS) spectroscopy was further carried out to probe the chemical state and local configuration of Bi HF. As shown in Fig. 2b, the shape and feature position of the X-ray absorption near edge structure (XANES) spectra of Bi HF and s-Bi HF aligned well with that of ref. Bi sample, in view of the fingerprint characteristics of XANES for structure identification, confirming the pure metallic Bi composition of Bi HF and s-Bi HF. Then, the least-squares Fourier-transformed extended X-ray absorption fine

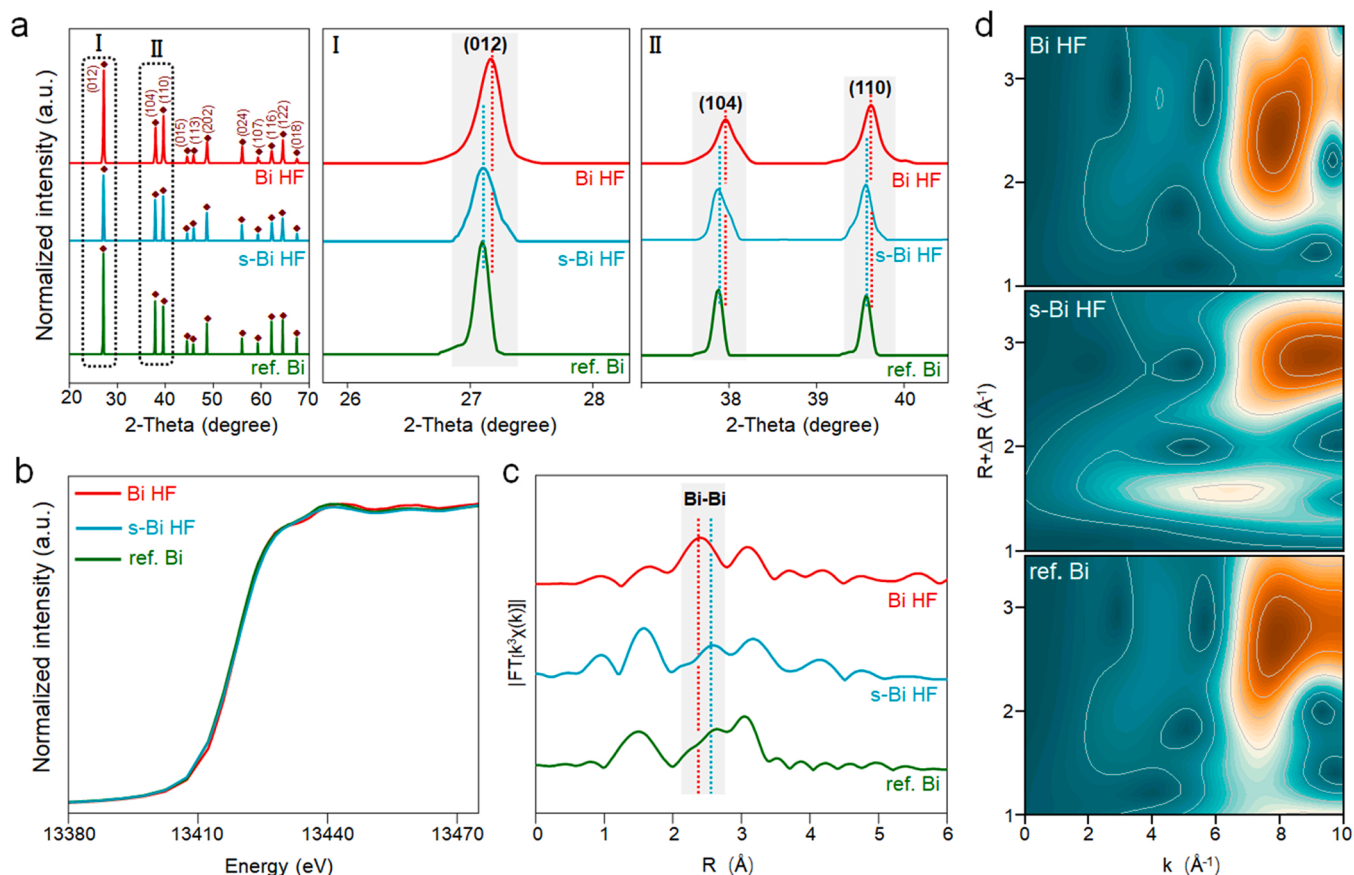


Fig. 2. (a) XRD patterns of ref. Bi, s-Bi HF and Bi HF, corresponding to enlarged XRD diffraction peaks of the (012), (104) and (110) planes. (b) Bi L₃-edge XANES spectra, (c) EXAFS and (d) wavelet transforms for the k_3 -weighted Bi K-edge EXAFS signals of ref. Bi, s-Bi HF and Bi HF.

structure (FT-EXAFS) spectra fitting was further analyzed to evaluate the quantitative coordination environments in Bi HF and s-Bi HF (Figs. 2c, S12 and Table S4). Besides metallic Bi, the Bi-O scattering peak at 1.8 Å with much weakened intensity implied the bismuth oxide species existed in Bi HF (Fig. S13), which was attributed to the surface partial oxidation of the Bi nanosheets in air. Furthermore, the Bi-Bi scattering path of Bi HF shows a shorter distance of 3.03 Å than that of ref. Bi sample (3.07 Å) and s-Bi HF (3.06 Å). In addition, the wavelet transform (WT) plot shows only one intensity maximum (Fig. 2d), corresponding to the Bi-Bi bond [52], while predominant intensity maximum at shorter bond length R was detected for Bi HF, these results implied a slight contraction of Bi-Bi bond length in Bi HF. This is probably due to the increased surface compressive strain, which is especially relevant for ultrathin structures and 2D nano materials [53].

3.1. Electrocatalytic CO₂RR performance

Bi HF array (Fig. S14a) comprising five tubes was used as a working electrode to evaluate its electrocatalytic activity of eCO₂RR in a custom-made flow H-type reaction cell system (Fig. S14b, c, d) with different concentration KHCO₃ aqueous solutions under ambient conditions, and the Bi HF GPE in 2.0 M KHCO₃ electrolyte solutions shows the best performance for formate production (Fig. S15). The KHCO₃ solutions with higher concentrations possessed the smaller solution resistances, which resulted in the increasing formate partial current densities (j_{formate}) from 0.5 M to 2.0 M, and Bi HF showed an ampere-level j_{formate} in 2.0 M (Fig. S15). At such high current density, when the KHCO₃ concentration further increased to 2.2 M, the higher coverage of K⁺ on the electrode surface affected the adsorption of CO₂ [54–56], resulting in a slight increase of HER. CO, H₂ and formate products were detected and

quantified by online gas chromatography and ¹H nuclear magnetic resonance (NMR) spectroscopy, respectively, and no other products were detected in the cathodic electrolyte after the electrochemical measurements. To validate the structural.

advantages of Bi HF, non-penetrating Bi HF (np-Bi HF) and s-Bi HF electrodes were further fabricated for comparison (Fig. S16). Fig. 3a shows the product distributions as their FEs including formate, CO and H₂ in 2 M KHCO₃ under applied potentials from – 0.59 V to – 1.26 V vs. RHE. It can be found that the H₂ FE always accounted for less than 6% and the CO FE was suppressed below 2%, and the formate FE slightly dropped from 95% at – 0.59 V down to 93% at – 1.26 V. And j_{formate} reached 1042 mA cm^{–2} at – 1.26 V over Bi HF (Fig. 3b and Fig. S17a), outperforming the previous prominent catalysts (Table S1). The cell voltages of Bi HF GPE in 2.0 M KHCO₃ at different current densities were lower compared with those of the prominent electrocatalysts [57,58]. In contrast, np-Bi HF delivered inferior CO₂ reduction performance with a dominant hydrogen evolution (Fig. S17b), more efficient eCO₂RR was realized in CO₂-penetrating mode applied at the same potential for identical electrode materials, which indicates the kinetics of CO₂ reduction were indeed restricted due to the limited mass transport from low CO₂ solubility. In addition, s-Bi HF exhibited a considerable capability of CO₂ to formate (Fig. S17c), but delivered FE_{formate} values only about 65% of those over Bi HF. Moreover, np-Bi HF also shows the higher selectivity for formate than s-Bi HF with non-penetrating mode (Fig. S18), implying that the contractive Bi-Bi bond induced by ultrasmall nanosheets may plays a significant role for the catalytic conversion of CO₂ to formate. Furthermore, electrochemical impedance spectroscopy (EIS) was used to investigate the electron transfer behaviors of the electrodes. The Nyquist plot of Fig. 3c showed that the Bi HF electrode has a smallest charge transfer resistance (R_{ct}) (0.3 Ω cm^{–2})

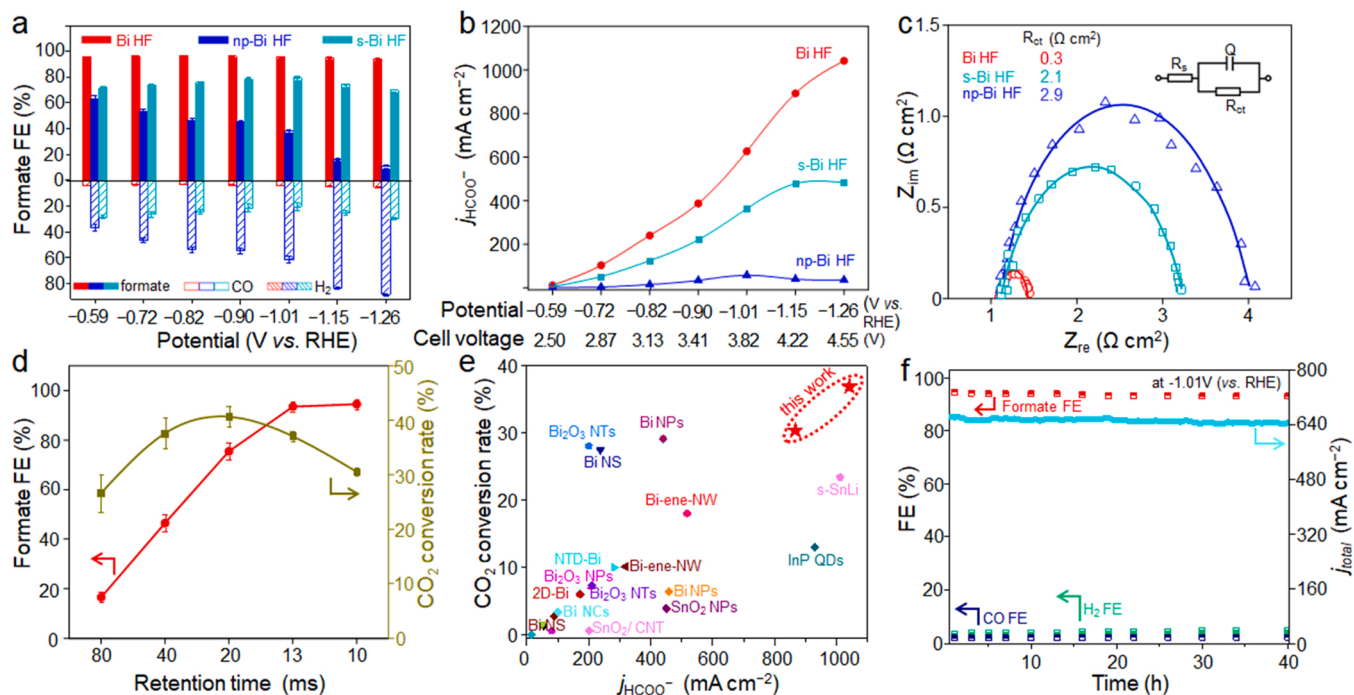


Fig. 3. Electrocatalytic CO₂RR performance in CO₂-saturated 2 M KHCO₃. (a) FE of formate, CO and H₂, (b) partial current densities of formate at different potentials and cell voltages for np-Bi HF, s-Bi HF and Bi HF. (c) EIS Nyquist plots at -1.01 V. (d) Formate faradaic efficiency and CO₂ conversion rate versus different retention time. (e) CO₂ conversion rates versus current densities, and the comparisons with reported prominent electrocatalysts (The geometric surface area of the catalysts were ≥ 1 cm²). (f) Stability test at -1.01 V.

compared with np-Bi HF ($2.9 \Omega \text{ cm}^{-2}$) and s-Bi HF ($2.1 \Omega \text{ cm}^{-2}$), this result manifests Bi HF exceeded np-Bi HF and s-Bi HF in the electrical conductivity, reflecting that Bi HF with abundant ultrasmall nanosheets facilitate the charge-transfer process [26].

Retention time, related to the main structural factor of GPE, affects gas reactants mass transfer by varying the CO₂ flow rates (Fig. S19). The variations of electrocatalytic performance by changing retention time over the Bi HF electrode for CO₂ reduction process have been clearly presented in Fig. 3d. The FE of formate shows a sharply increase with the decline of retention time under the constant current density of 1.13 A cm^{-2} and then reached the threshold, this is probably because the CO₂ feeding is insufficient under the long retention time until ample CO₂ feeding was achieved. While the CO₂ conversion rate presents Volcanic type trend with respect to retention time, in consideration of carbon utilization efficiency in electrocatalytic process, we can conclude that Bi HF exhibits optimal activity with a retention time of 13 ms. We further evaluate the conversion rate of Bi HF, np-Bi HF and s-Bi HF under different potential at an optimal retention time. Bi HF showed highest the CO₂ conversion rate under all applied potential and it reached the maximum conversion rate of 37% at -1.26 V (Fig. S20). Furthermore, the ultra-high j_{formate} values were also realized over Bi HF and the FE of formate still keeps over 90%, to the best of our knowledge, which was one of the highest reported conversion rates and largest current density for formate under keeping high selectivity (90%) at a mild condition (Fig. 3e), displaying great potential for large-scale application.

Further durability assessment of Bi HF was carried out at -1.01 V, and the formate FE slightly decreased from 95% to 93% and the total current densities from 663 to 644 mA cm^{−2} during the 40-hour electrolysis (Fig. 3f). The ICP-OES measurements of the outlet electrolyte indicated that no Bi dissolution was found under the eCO₂RR conditions. Post-reaction XRD showed that the composition of Bi HF was same to that before electrolysis (Fig. S21), and the surface morphology of nanosheets was also similar to initial Bi HF (Fig. S22). The feeding CO₂ pressure inside hollow fiber was 4.2 bar (Fig. S14b) and remained constant during the 40 h electrolysis test. And the pore sizes and

porosity (Fig. S23 and Table S5) of Bi HF were highly similar before and after reaction, implying the stable pore structures of Bi HF. Moreover, the postreaction XRD (Figs. S20 and S24) and EXAFs (Fig. S25) results revealed the unchanged compositions of Bi HF after the 40 h electrolysis, and the contractive Bi-Bi bond also remained stable (Fig. 24). Furthermore, the unique self-supported Bi GPE consists of only a single active component with an abundant surface area and tunable pore structure and gaseous CO₂ was forced to penetrate the porous channels to make good contact with the catalyst and electrolyte, promoting CO₂ electroreduction at the gas-catalyst-liquid three-phase boundary [42,59,60], which can effectively avoid flooding generated from GDEs, accounting for the stable electrocatalytic performance of Bi HF.

3.2. CO₂ penetration effect

It is generally known that the electrocatalytic reaction of high current densities needs sufficient supply of gaseous reactants to the active sites, thus the gaseous reactants feeding manner from different electrode structure plays a crucial role in efficient CO₂ electroreduction. As is shown in Fig. 4a, the ultra-high j_{formate} values were realized over Bi HF and s-Bi HF with CO₂-penetrating mode, although the experimental values were still lower than those of $j_{\text{formate, limit(gas)}}$ as an extremely ideal case, they even far outperforming the $j_{\text{formate, limit(sol)}}$, which is about 94 mA cm^{-2} according to the 100% conversion of dissolved CO₂ in aqueous electrolytes with a saturated concentration of 34 mM [61]. In sharp contrast, np-Bi HF, as similar with planar electrode, showed maximum j_{formate} of 47 mA cm^{-2} , these results reveal that CO₂-penetrating mode is uniquely superior to the non-penetrating mode. As is shown in Fig. 4b, Bi HF with CO₂-penetrating mode offered a scenario that CO₂ were high dispersion and compulsively interacted with surface active nanosheet sites, thereby maintaining extremely high local CO₂ concentration nearby triphasic interface sites to meet the fast production rate. However, for non-penetrating mode (Fig. 4c), the reactants are supplied from the diffusion of soluble gas in bulk electrolyte [62,63], and thus the reaction is mass transport limited because the diffusion of

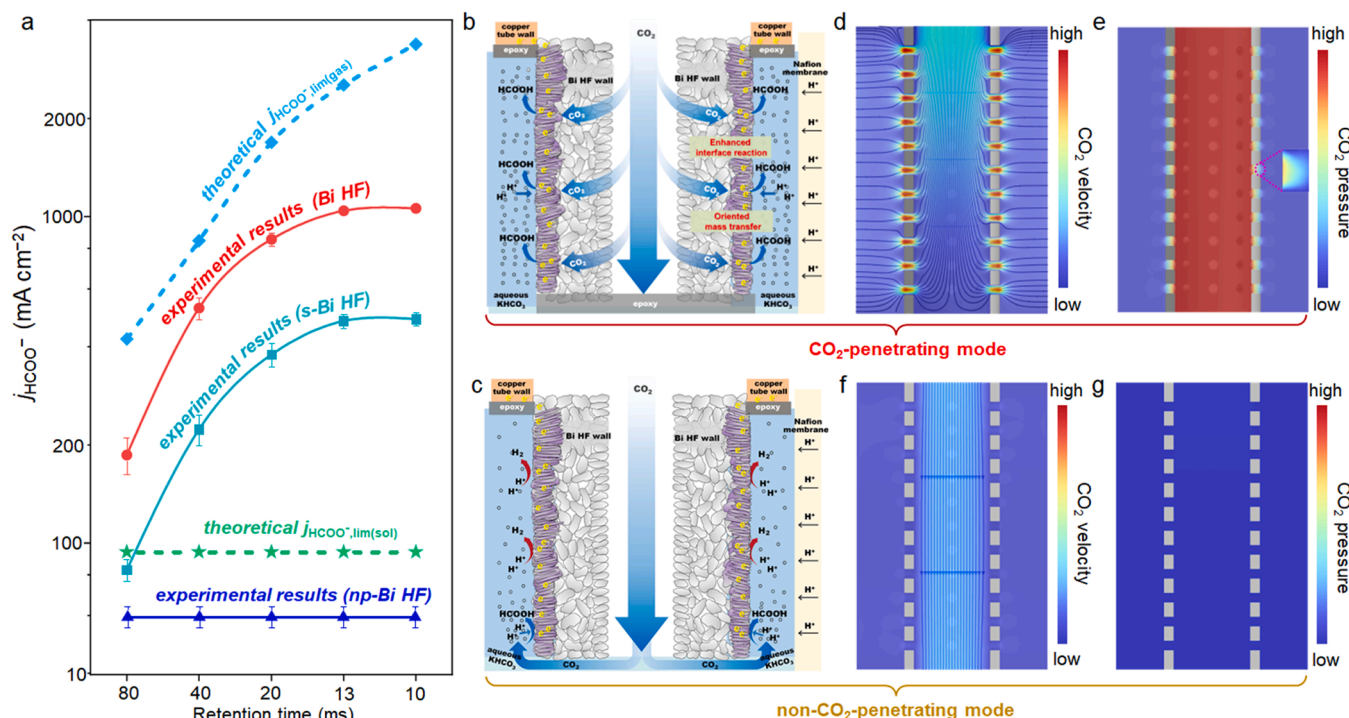


Fig. 4. CO₂ penetrating effect studies. (a) Comparison of experimental j values with different theoretical limits $j_{\text{formate limit(gas)}}$ and $j_{\text{formate limit(sol)}}$ at different CO₂ retention time. (b) Bi HF with CO₂-penetrating mode. (c) Bi HF with non-CO₂-penetrating mode. Simulation results of the velocity (d), (f) and pressure (e), (g) field distribution in CO₂-penetrating mode and non-CO₂-penetrating mode by COMSOL Multiphysics, respectively.

gaseous reactants to the active layer interface is insufficient. Hence, the CO₂-penetrating design for hollow fiber broke the constraint of CO₂ mass diffusion and enhanced triphasic interface reactions and mass transfers, resulting in significant CO₂ electroreduction.

To better understand the CO₂ penetrating effect, CO₂ feeding distribution around the Bi HF electrode surface was simulated by building a 3D model (Fig. S26). The finite element analysis (FEA) simulation results of the velocity and pressure field of penetrating CO₂ in the Bi HF verified the CO₂ velocity inside the microchannels was faster, and thus the CO₂ bubble flow rushed out from the microchannels and spread around the active nanosheets (Fig. 4d), meanwhile the maximum pressure value reached in the microchannels at first and then decreased gradually outward, the local high-pressure CO₂ was achieved on the surface of Bi HF (Fig. 4e). Given the pressure was positively correlated with the CO₂ concentration [64], these results indicated that the CO₂ feeding to the active nanosheets surface was sufficient and continuous, which was regarded as more benefitting to eCO₂RR. Moreover, the direction of CO₂ flow from hollow fiber inside to outside facilitated the departures and diffusion of as-produced formate from the electrode region [65], avoiding the possible delay and accumulation. However, Fig. 4f displays the CO₂ flowed through the hollow fiber to the bulk electrolyte and little gas penetrated through the wall of the hollow fiber, resulting in the destitute CO₂ pressure near Bi HF surface (Fig. 4g), corresponding to np-Bi HF. Hence, Bi HF with CO₂-penetrating mode realized the sufficient supply at triphasic interfaces and facilitated CO₂ reduction kinetics reaching ampere-level current density.

3.3. Contraction effect of Bi-Bi bond

Density functional theory (DFT) calculations were performed to further investigate how the contractive Bi-Bi bond of Bi HF electrode enhances the eCO₂RR performance, from precious research, it is generally known that the formation of *OCHO immediate is the energetically most favorable pathway after the first protonation of CO₂ for formate production [66]. Herein, the calculations were based on the Bi

(012), (104) and (110) facets model (Fig. S27), which was consistent with the aboved structural characterization, so as to evaluate the ability of generating *OCHO immediate in the absence/presence of Bi-Bi bond contraction (Fig. S28). As is shown in Fig. 5a, with respect to the Bi (012) facet, the ΔG for the formation of *OCHO intermediate via the first proton-electron transfer with the ideal Bi-Bi bond and contractive Bi-Bi bond is 0.09 eV and 0.05 eV, respectively. Moreover, the ΔG for the formation of *H was 0.31 eV on the Bi (012) surface with contractive Bi-Bi bond, which was higher than that (0.26 eV) on the Bi (012) facet with ideal Bi-Bi bond, displaying significant suppression for the formation of H₂ on the Bi (012) facet at the presence of contractive Bi-Bi bond. Thus, the contractive Bi-Bi bond decreased activation energy barrier in the first protonation of CO₂, while exacerbating the HER barrier greatly, implying that a more favorable pathway to form *OCHO intermediate, rather than *H. Furthermore, the ΔG for the formation of *OCHO and *H on the (104) and (110) facets of both ideal and contractive Bi-Bi bond were similar, indicating the insensitivity of these facets to the contraction of Bi-Bi bond length. Hence, the DFT results confirmed that the Bi (012) facet with contractive Bi-Bi bond boosted the electrocatalytic activity of the Bi HF electrode via the suppression of the HER reaction and the simultaneous enhancement of the eCO₂RR to formate reaction.

Consequently, for Bi HF GPE, enhanced triphasic interface reactions and mass transfers from sufficient and targeted CO₂ feeding meet the production rate under high current densities with fast electron transfer kinetic, moreover, the contractive Bi-Bi bond from ultrasmall nanosheets provides abundant active sites promoted the selectivity, the synergetic combination of the two merits resulted in high current densities of Bi HF (Figs. 5b and S29), which are responsible for the superior performance for eCO₂RR.

4. Conclusion

In this study, we present a high-performance Bi HF as the GPE for CO₂ electroreduction to formate. The CO₂-penetrating manner broke the constraint of CO₂ mass diffusions and heightened triphasic interface

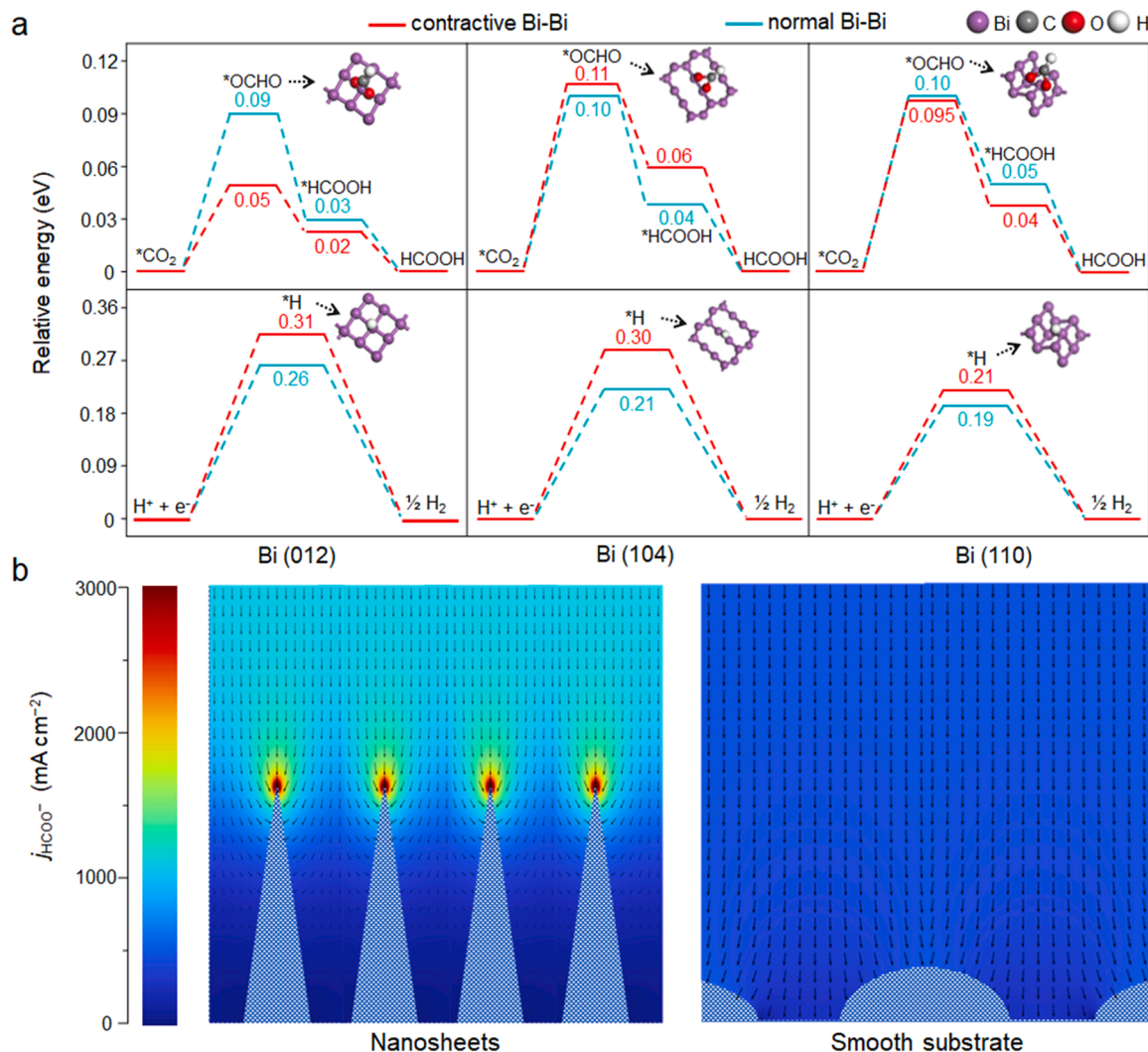


Fig. 5. (a) Free-energy profiles for formate and H₂ productions over Bi (012), (104) and (110) planes with contractive and normal Bi-Bi bonds respectively. (b) Simulation results of the formate current densities distribution over the Bi HF and s-BiHF surface by COMSOL Multiphysics.

reactions and reduction kinetics. The contractive Bi-Bi bond for Bi HF greatly improved the formate selectivity by decreasing activation energy barrier of *OCHO key intermediate. The high formate FE (93%) and the large current densities (1.13 A cm⁻²) with high CO₂ conversion rate (37%) were achieved under mild conditions. This work opens an avenue for great promotions of CO₂ electrocatalytic performance in aqueous solutions by the rational GPE design.

CRediT authorship contribution statement

Aohui Chen: Experiments, Data curation, Writing – original draft. **Xiao Dong:** Experiments, Data curation. **Jianing Mao:** Experiments, Data curation. **Wei Chen:** Conceptualization, Data curation, Writing – review & editing, Supervision. **Chang Zhu:** Data curation. **Shoujie Li:** Data curation. **Gangfeng Wu:** Data curation. **Yiheng Wei:** Data curation. **Xiaohu Liu:** Data curation. **Guihua Li:** Data curation. **Yanfang Song:** Data curation. **Zheng Jiang:** Supervision. **Wei Wei:** Supervision. **Yuhan Sun:** Supervision.

Declaration of Competing Interest

The authors declare that they have no known competing financial interests or personal relationships that could have appeared to influence the work reported in this paper.

Data availability

Data will be made available on request.

Acknowledgements

This work was financially supported by the Ministry of Science and Technology of China (2022YFA1504604, National Key R&D Program of China), the National Natural Science Foundation of China (nos. 91745114, 21802160), the “Transformational Technologies for Clean Energy and Demonstration”, Strategic Priority Research Program of the Chinese Academy of Sciences (no. XDA 21000000), the Hundred Talents Program of Chinese Academy of Sciences (no. 2060299), the Youth Innovation Promotion Association of the Chinese Academy of Sciences (no. E224301401), Shanghai Sailing Program (no. 18YF1425700), Shanghai Pujiang Program (no. 20PJ1415200), the Outstanding Young Talent Project of Shanghai Advanced Research Institute, the Chinese Academy of Sciences (no. E254991ZZ1), the Foundation of Key Laboratory of Low-Carbon Conversion Science & Engineering, Shanghai Advanced Research Institute, Chinese Academy of Sciences (no. KLLCCSE-202207Z, SARI, CAS), Shanghai Functional Platform for Innovation Low Carbon Technology, and the Major Project of the Science and Technology Department of Inner Mongolia (no. 2021ZD0020). The authors appreciate the BL14W1 beamline of Shanghai Synchrotron

Radiation Facility (SSRF), Shanghai, China.

Appendix A. Supporting information

Supplementary data associated with this article can be found in the online version at doi:10.1016/j.apcatb.2023.122768.

References

- [1] S. Mallapaty, How China could be carbon neutral by mid-century, *Nature* 586 (2020) 482–483.
- [2] S.M. Joradan, C. Wang, Electrocatalytic conversion of carbon dioxide for the Paris goals, *Nat. Catal.* 4 (2021) 915–920.
- [3] L. Han, S. Song, M. Liu, S. Yao, Z. Liang, H. Cheng, Z. Ren, W. Liu, R. Lin, G. Qi, X. Liu, Q. Wu, J. Luo, H.L. Xin, Stable and Efficient Single-Atom Zn Catalyst for CO₂ Reduction to CH₄, *J. Am. Chem. Soc.* 142 (2020) 12563–12567.
- [4] J. Gu, C.-S. Hsu, L. Bai, H.M. Chen, X. Hu, Atomically dispersed Fe³⁺ sites catalyze efficient CO₂ electroreduction to CO, *Science* 364 (2019) 1091–1094.
- [5] Y. Wu, Z. Jiang, X. Lu, Y. Liang, H. Wang, Domino electroreduction of CO₂ to methanol on a molecular catalyst, *Nature* 575 (2019) 639–642.
- [6] C. Xia, P. Zhu, Q. Jiang, Y. Pan, W. Liang, E. Stavitsk, H.N. Alshareef, H. Wang, Continuous production of pure liquid fuel solutions via electrocatalytic CO₂ reduction using solid-electrolyte devices, *Nat. Energy* 4 (2019) 776–785.
- [7] H. Xu, D. Rebolgar, H. He, L. Chong, Y. Liu, C. J. Sun, T. Li, J.V. Muntean, R. E. Winans, D.-J. Liu, T. Xu, Highly selective electrocatalytic CO₂ reduction to ethanol by metallic clusters dynamically formed from atomically dispersed copper, *Nat. Energy* 5 (2020) 623–632.
- [8] F.P.G. de Arquer, F.P.G. Dinh, C.T. Ozden, A. Wicks, J. McCallum, C. Kirmani, A. R. Nam, D.H. Gabardo, C. Seifitokaldani, A. Wang, X. Li, Y.G.C. Li, F.W. Edwards, J. Richter, L.J. Thorpe, S.J. Sinton, D. Sargent, E. H. CO₂ electrolysis to multicarbon products at activities greater than 1 A cm⁻², *Science* 367 (2020) 661–666.
- [9] W. Ma, S. Xie, T. Liu, Q. Fan, J. Ye, F. Sun, Z. Jiang, Q. Zhang, J. Cheng, Y. Wang, Electrocatalytic reduction of CO₂ to ethylene and ethanol through hydrogen-assisted C–C coupling over fluorine-modified copper, *Nat. Catal.* 3 (2020) 478–487.
- [10] T. Zheng, M. Zhang, L. Wu, S. Guo, X. Liu, J. Zhao, W. Xue, J. Li, C. Liu, X. Li, Q. Jiang, J. Bao, J. Zeng, T. Yu, C. Xia, Upcycling CO₂ into energy-rich long-chain compounds via electrochemical and metabolic engineering, *Nat. Catal.* 5 (2022) 388–396.
- [11] G. Wang, J. Chen, Y. Ding, P. Cai, L. Yi, Y. Li, C. Tu, Y. Hou, Z. Wen, L. Dai, Electrocatalysis for CO₂ conversion: from fundamentals to value-added products, *Chem. Soc. Rev.* 50 (2021) 4993–5061.
- [12] O.S. Bushuyev, P. De Luna, C.T. Dinh, L. Tao, G. Saur, J. Van De Lagemaat, S. O. Kelley, E.H. Sargent, What Should We Make with CO₂ and How Can We Make It? *Joule* 2 (2018) 825–832.
- [13] R.I. Masel, Z. Liu, H. Yang, J.J. Kaczur, D. Carrillo, S. Ren, D. Salvatore, C. P. Berlinguette, An industrial perspective on catalysts for low-temperature CO₂ electrolysis, *Nat. Nanotechnol.* 16 (2021) 118–128.
- [14] S. Nitopi, E. Bertheussen, S.B. Scott, J. Liu, A.K. Engstfeld, S. Horch, B. Seger, I.E. L. Stephens, K. Chan, C. Hahn, J.K. Nørskov, T.F. Jaramillo, I. Chorkendorff, Progress and Perspectives of Electrochemical CO₂ Reduction on Copper in Aqueous Electrolyte, *Chem. Rev.* 119 (2019) 7610–7672.
- [15] Y. Xiong, J. Dong, Z.-Q. Huang, P. Xin, W. Chen, Y. Wang, Z. Li, Z. Jin, W. Xing, Z. Zhuang, J. Ye, X. Wei, R. Cao, L. Gu, S. Sun, L. Zhuang, X. Chen, H. Yang, C. Chen, Q. Peng, C.-R. Chang, D. Wang, Y. Li, Single-atom Rh/N-doped carbon electrocatalyst for formic acid oxidation, *Nat. Nanotechnol.* 15 (2020) 390–397.
- [16] Z. Li, Y. Chen, S. Ji, Y. Tang, W. Chen, A. Li, J. Zhao, Y. Xiong, Y. Wu, Y. Gong, T. Yao, W. Liu, L. Zheng, J. Dong, Y. Wang, Z. Zhuang, W. Xing, C.-T. He, C. Peng, W.-C. Cheong, Q. Li, M. Zhang, Z. Chen, N. Fu, X. Gao, W. Zhu, J. Wan, J. Zhang, L. Gu, S. Wei, P. Hu, J. Luo, J. Li, C. Chen, Q. Peng, X. Duan, Y. Huang, X.-M. Chen, D. Wang, Y. Li, Iridium single-atom catalyst on nitrogen-doped carbon for formic acid oxidation synthesized using a general host–guest strategy, *Nat. Chem.* 12 (2020) 764–772.
- [17] J. Ding, Z. Liu, X. Liu, B. Liu, J. Liu, Y. Deng, X. Han, W. Hu, C. Zhong, Tunable Periodically Ordered Mesoporosity in Palladium Membranes Enables Exceptional Enhancement of Intrinsic Electrocatalytic Activity for Formic Acid Oxidation, *Angew. Chem. Int. Ed.* 59 (2020) 5092–5101.
- [18] L. Fan, C. Xia, P. Zhu, Y. Lu, H. Wang, Electrochemical CO₂ reduction to high-concentration pure formic acid solutions in an all-solid-state reactor, *Nat. Commun.* 11 (2020) 3633.
- [19] T. Zheng, C. Liu, C. Guo, M. Zhang, X. Li, Q. Jiang, W. Xue, H. Li, A. Li, C.-W. Pao, J. Xiao, C. Xia, J. Zeng, Copper-catalysed exclusive CO₂ to pure formic acid conversion via single-atom alloying, *Nat. Nanotechnol.* 16 (2021) 1386–1393.
- [20] H. Cheng, S. Liu, J. Zhang, T. Zhou, N. Zhang, X.-S. Zheng, W. Chu, Z. Hu, C. Wu, Y. Xie, Surface nitrogen-injection engineering for high formation rate of CO₂ reduction to formate, *Nano Lett.* 20 (2020) 6097–6103.
- [21] S. Yan, C. Peng, C. Yang, Y. Chen, J. Zhang, A. Guan, X. Lv, H. Wang, Z. Wang, T. K. Sham, Q. Han, G. Zheng, Electron localization and lattice strain induced by surface lithium doping enable ampere-level electrosynthesis of formate from CO₂, *Angew. Chem. Int. Ed.* 60 (2021) 25741–25745.
- [22] Z. Xing, X. Hu, X. Feng, Tuning the microenvironment in gas-diffusion electrodes enables high-rate CO₂ electrolysis to formate, *ACS Energy Lett.* 6 (2021) 1694–1702.
- [23] D. Xia, H. Yu, H. Xie, P. Huang, R. Menzel, M.M. Titirici, G. Chai, Recent progress of Bi-based electrocatalysts for electrocatalytic CO₂ reduction, *Nanoscale* 14 (2022) 7957–7973.
- [24] S. He, F. Ni, Y. Ji, L. Wang, Y. Wen, H. Bai, G. Liu, Y. Zhang, Y. Li, B. Zhang, H. Peng, The p-Orbital Delocalization of Main-Group Metals to Boost CO₂ Electroreduction, *Angew. Chem. Int. Ed.* 57 (2018) 16114–16119.
- [25] F. Yang, A.O. Elnabawy, R. Schimmenti, P. Song, J. Wang, Z. Peng, S. Yao, R. Deng, S. Song, Y. Lin, M. Mavrikakis, W. Xu, Bismuthene for highly efficient carbon dioxide electroreduction reaction, *Nat. Commun.* 11 (2020) 1088.
- [26] J. Fan, X. Zhao, X. Mao, J. Xu, N. Han, H. Yang, B. Pan, Y. Li, L. Wang, Y. Li, Large-area vertically aligned bismuthene nanosheet arrays from galvanic replacement reaction for efficient electrochemical CO₂ conversion, *Adv. Mater.* 33 (2021) 2100910.
- [27] H. Yang, N. Han, J. Deng, J. Wu, Y. Wang, Y. Hu, P. Ding, Y. Li, Y. Li, J. Lu, Selective CO₂ Reduction on 2D Mesoporous Bi Nanosheets, *Adv. Energy Mater.* 8 (2018) 1801536.
- [28] N. Han, Y. Wang, H. Yang, J. Deng, J. Wu, Y. Li, Y. Li, Ultrathin bismuth nanosheets from in situ topotactic transformation for selective electrocatalytic CO₂ reduction to formate, *Nat. Commun.* 9 (2018) 1320.
- [29] X. Liu, S. Zhang, S. Guo, B. Cai, S.A. Yang, F. Shan, M. Pumera, H. Zeng, Advances of 2D bismuth in energy sciences, *Chem. Soc. Rev.* 49 (2020) 263–285.
- [30] J.J. Lv, M. Jouny, W. Luc, W. Zhu, J.J. Zhu, F. Jiao, A. Highly Porous Copper Electrocatalyst for Carbon Dioxide Reduction, *Adv. Mater.* 30 (2018) 1803111.
- [31] M. Liu, Y. Pang, B. Zhang, P. De Luna, O. Voznyy, J. Xu, X. Zheng, C.T. Dinh, F. Fan, C. Cao, F.P.G. de Arquer, T.S. Safaei, A. Mephram, A. Klinkova, E. Kumacheva, T. Filleter, D. Sinton, S.O. Kelley, E.H. Sargent, Enhanced electrocatalytic CO₂ reduction via field-induced reagent concentration, in: *Nature*, 537, 2016, pp. 382–386.
- [32] C.-T. Dinh, T. Burdyny, M.G. Kibria, A. Seifitokaldani, C.M. Gabardo, P. García De Arquer, F. A. Kiani, J.P. Edwards, P. De Luna, O.S. Bushuyev, C. Zou, R. Quintero-Bermudez, Y. Pang, D. Sinton, E.H. Sargent, CO₂ electroreduction to ethylene via hydroxide-mediated copper catalysis at an abrupt interface, *Science* 360 (2018) 783–787.
- [33] T.N. Nguyen, C.-T. Dinh, Gas diffusion electrode design for electrochemical carbon dioxide reduction, *Chem. Soc. Rev.* 49 (2020) 7488–7504.
- [34] F.P. García De Arquer, O.S. Bushuyev, P. De Luna, C.-T. Dinh, A. Seifitokaldani, M. I. Saidminov, C.-S. Tan, L.N. Quan, A. Proppe, M.G. Kibria, S.O. Kelley, D. Sinton, E.H. Sargent, 2D metal oxyhalide-derived catalysts for efficient CO₂ electroreduction, *Adv. Mater.* 30 (2018) 1802858.
- [35] Q. Gong, P. Ding, M. Xu, X. Zhu, M. Wang, J. Deng, Q. Ma, N. Han, Y. Zhu, J. Lu, Z. Feng, Y. Li, W. Zhou, Y. Li, Structural defects on converted bismuth oxide nanotubes enable highly active electrocatalysis of carbon dioxide reduction, *Nat. Commun.* 10 (2019) 2807.
- [36] L. Yi, J. Chen, P. Shao, J. Huang, X. Peng, J. Li, G. Wang, C. Zhang, Z. Wen, Molten-Salt-Assisted Synthesis of Bismuth Nanosheets for Long-term Continuous Electrocatalytic Conversion of CO₂ to Formate, *Angew. Chem. Int. Ed.* 59 (2020) 20112–20119.
- [37] Y. Li, J. Chen, S. Chen, X. Liao, T. Zhao, F. Cheng, H. Wang, In Situ Confined Growth of Bismuth Nanoribbons with Active and Robust Edge Sites for Boosted CO₂ Electroreduction, *ACS Energy Lett.* 7 (2022) 1454–1461.
- [38] M. Zhang, W. Wei, S. Zhou, D.-D. Ma, A. Cao, X.-T. Wu, Q.-L. Zhu, Engineering a conductive network of atomically thin bismuthene with rich defects enables CO₂ reduction to formate with industry-compatible current densities and stability, *Energy Environ. Sci.* 14 (2021) 4998–5008.
- [39] Y. Qiao, W. Lai, K. Huang, T. Yu, Q. Wang, L. Gao, Z. Yang, Z. Ma, T. Sun, M. Liu, C. Lian, H. Huang, Engineering the Local Microenvironment over Bi Nanosheets for Highly Selective Electrocatalytic Conversion of CO₂ to HCOOH in Strong Acid, *ACS Catal.* 12 (2022) 2357–2364.
- [40] H. Rabiee, L. Ge, X. Zhang, S. Hu, M. Li, Z. Yuan, Gas diffusion electrodes (GDEs) for electrochemical reduction of carbon dioxide, carbon monoxide, and dinitrogen to value-added products: a review, *Energy Environ. Sci.* 14 (2021) 1959–2008.
- [41] R. Kas, K.K. Hummadi, R. Kortlever, P. de Wit, A. Milbrat, M.W. Luiten-Olieman, N. E. Benes, M.T. Koper, G. Mul, Three-dimensional porous hollow fibre copper electrodes for efficient and high-rate electrochemical carbon dioxide reduction, *Nat. Commun.* 7 (2016) 10748.
- [42] S. Li, W. Chen, X. Dong, C. Zhu, A. Chen, Y. Song, G. Li, W. Wei, Y. Sun, Hierarchical micro/nanostructured silver hollow fiber boosts electroreduction of carbon dioxide, *Nat. Commun.* 13 (2022) 3080.
- [43] C. Zhu, G. Shen, W. Chen, X. Dong, G. Li, Y. Song, W. Wei, Y. Sun, Copper hollow fiber electrode for efficient CO₂ electroreduction, *J. Power Sources* 495 (2021), 229814.
- [44] H. Rabiee, L. Ge, X. Zhang, S. Hu, M. Li, S. Smart, Z. Zhu, Z. Yuan, Shape-tuned electrodeposition of bismuth-based nanosheets on flow-through hollow fiber gas diffusion electrode for high-efficiency CO₂ reduction to formate, *Appl. Catal. B: Environ.* 286 (2021), 119945.
- [45] H. Rabiee, L. Ge, X. Zhang, S. Hu, M. Li, S. Smart, Z. Zhu, H. Wang, Z. Yuan, Stand-alone asymmetric hollow fiber gas-diffusion electrodes with distinguished bronze phases for high-efficiency CO₂ electrochemical reduction, *Appl. Catal. B: Environ.* 298 (2021), 120538.
- [46] B. Chen, J. Xu, J. Zou, D. Liu, Y. Situ, H. Huang, Formate selective CO₂ electrochemical reduction with a hydrogen reduction suppressing bronze alloy hollow fiber electrode, *ChemSusChem* 13 (2020) 6594–6601.
- [47] S. Praveen, S. Veeralingam, S. Badhulika, A Flexible Self-Powered UV Photodetector and Optical UV Filter Based on β -Bi₂O₃/SnO₂ Quantum Dots Schottky Heterojunction, *Adv. Mater. Interfaces* 8 (2021) 2100373.

- [48] F.D. Hardcastle, I.E. Wachs, The molecular structure of bismuth oxide by Raman spectroscopy, *J. Solid State Chem.* 97 (1992) 319–331.
- [49] A.A. Othman, M.A. Osman, E.M.M. Ibrahim, M.A. Ali, Sonochemically synthesized ZnO nanosheets and nanorods: Annealing temperature effects on the structure, and optical properties, *Ceram. Int.* 43 (2017) 527–533.
- [50] U. Holzwarth, N. Gibson, The Scherrer equation versus the “Debye-Scherrer equation”, *Nat. Nanotechnol.* 6 (2011) 534.
- [51] F. Hu, J. Chen, Y. Peng, H. Song, K. Li, J. Li, Novel nanowire self-assembled hierarchical CeO₂ microspheres for low temperature toluene catalytic combustion, *Chem. Eng. J.* 331 (2018) 425–434.
- [52] Y. Liu, Z.X. Lou, X. Wu, B. Mei, J. Chen, J.Y. Zhao, J. Li, H.Y. Yuan, M. Zhu, S. Dai, C. Sun, P.F. Liu, Z. Jiang, H.G. Yang, Molecularly Distorted Local Structure in Bi₂CuO₄ Oxide to Stabilize Lattice Oxygen for Efficient Formate Electrosynthesis, *Adv. Mater.* 34 (2022) 2202568.
- [53] H.N. Nong, T. Reier, H.-S. Oh, M. Glicch, P. Paciok, T.H.T. Vu, D. Teschner, M. Heggen, V. Petkov, R. Schlögl, T. Jones, P. Strasser, A unique oxygen ligand environment facilitates water oxidation in hole-doped IrNiOx core-shell electrocatalysts, *Nat. Catal.* 1 (2018) 841–851.
- [54] D. Bohra, J.H. Chaudhry, T. Burdyny, E.A. Pidko, W.A. Smith, Modeling the electrical double layer to understand the reaction environment in a CO₂ electrocatalytic system, *Energy Environ. Sci.* 12 (2019) 3380–3389.
- [55] B. Endrődi, et al., Operando cathode activation with alkali metal cations for high current density operation of water-fed zero-gap carbon dioxide electrolyzers, *Nat. Energy* 6 (2021) 439–448.
- [56] A. Ozden, J. Li, S. Kandambeth, X.-Y. Li, S. Liu, O. Shekhah, P. Ou, Y. Zou Finrock, Y.-K. Wang, T. Alkayyali, F. Pelayo García De Arquer, V.S. Kale, P.M. Bhatt, A. H. Ip, M. Eddaoudi, E.H. Sargent, D. Sinton, Energy- and carbon-efficient CO₂/CO electrolysis to multicarbon products via asymmetric ion migration-adsorption, *Nat. Energy* (2023) 2, <https://doi.org/10.1038/s41560-022-01188->.
- [57] Y. Chen, A. Vise, W.E. Klein, F.C. Cetinbas, D.J. Myers, W.A. Smith, T.G. Deutsch, K.C. Neyerlin, A. Robust, Scalable Platform for the Electrochemical Conversion of CO₂ to Formate: Identifying Pathways to Higher Energy Efficiencies, *ACS Energy Lett.* 5 (2020) 1825–1833.
- [58] T. Li, E.W. Lees, Z. Zhang, C.P. Berlinguette, Conversion of bicarbonate to formate in an electrochemical flow reactor, *ACS Energy Lett.* 5 (2020) 2624–2630.
- [59] C. Zhu, Y. Song, X. Dong, G. Li, A. Chen, W. Chen, G. Wu, S. Li, W. Wei, Y. Sun, Ampere-level CO₂ reduction to multicarbon products over a copper gas penetration electrode, *Energy Environ. Sci.* 15 (2022) 5391–5404.
- [60] Y. Song, X. Dong, W. Chen, W. Wei, Hollow-fiber gas penetration electrodes efficiently produce renewable synthetic fuels, *Front. Energy* 16 (2022) 700–705.
- [61] C. Yan, H. Li, Y. Ye, H. Wu, F. Cai, R. Si, J. Xiao, S. Miao, S. Xie, F. Yang, Y. Li, G. Wang, X. Bao, Coordinatively unsaturated nickel–nitrogen sites towards selective and high-rate CO₂ electroreduction, *Energy Environ. Sci.* 11 (2018) 1204–1210.
- [62] D.M. Weekes, D.A. Salvatore, A. Reyes, A. Huang, C.P. Berlinguette, Electrolytic CO₂ reduction in a flow cell, *Acc. Chem. Res.* 51 (2018) 910–918.
- [63] T. Burdyny, W.A. Smith, CO₂ reduction on gas-diffusion electrodes and why catalytic performance must be assessed at commercially-relevant conditions, *Energy Environ. Sci.* 12 (2019) 1442–1453.
- [64] H. Wang, C. Wang, X. Wang, F. Sun, Effects of carbon concentration and gas pressure with hydrogen-rich gas chemistry on synthesis and characterizations of HFCVD diamond films on WC-Co substrates, *Surf. Coat. Technol.* 409 (2021), 126839.
- [65] T. Burdyny, P.J. Graham, Y. Pang, C.T. Dinh, M. Liu, E.H. Sargent, D. Sinton, Nanomorphology-enhanced gas-evolution intensifies CO₂ reduction electrochemistry, *ACS Sustain. Chem. Eng.* 5 (2017) 4031–4040.
- [66] J.H. Koh, D.H. Won, T. Eom, N.-K. Kim, K.D. Jung, H. Kim, Y.J. Hwang, B.K. Min, Facile CO₂ electro-reduction to formate via oxygen bidentate intermediate stabilized by high-index planes of bi dendrite catalyst, *ACS Catal.* 7 (2017) 5071–5077.